Geoscience Frontiers 13 (2022) 101270

HOSTED BY

ELSEVIER

Contents lists available at ScienceDirect

Geoscience Frontiers

journal homepage: www.elsevier.com/locate/gsf

Research Paper

The effect of oxygen fugacity on ionic conductivity in olivine

Hongzhan Fei [a,*], Tomoo Katsura [a,b]

[a] Bayerisches Geoinstitut, University of Bayreuth, 95447 Bayreuth, Germany
[b] Center for High Pressure Science and Technology Advanced Research, Beijing 100097, China

ARTICLE INFO

Article history:
Received 1 March 2021
Revised 24 May 2021
Accepted 8 July 2021
Available online 13 July 2021
Handling Editor: R.M. Palin

Keywords:
Olivine
Ionic conductivity
Crystal structure
Oxygen fugacity
Upper mantle

ABSTRACT

The oxygen fugacity (f_{O_2}) may affect the ionic conductivity of olivine under upper mantle conditions because Mg vacancies can be produced in the crystal structure by the oxidization of iron from Fe^{2+} to Fe^{3+}. Here we investigated olivine ionic conductivity at 4 GPa, as a function of temperature, crystallographic orientation, and oxygen fugacity, corresponding to the topmost asthenospheric conditions. The results demonstrate that the ionic conductivity is insensitive to f_{O_2} under relatively reduced conditions (f_{O_2} below Re-ReO_2 buffer), whereas it has a clear f_{O_2}-dependence under relatively oxidized conditions (f_{O_2} around the magnetite-hematite buffer). The ionic conduction in olivine may contribute significantly to the conductivity anomaly in the topmost asthenosphere especially at relatively oxidized conditions.

1. Introduction

Olivine, the most abundant mineral in the upper mantle constituting more than 55 vol%, has three major electrical-conductivity mechanisms. The first one is the small-polaron conduction (σ_{sp}). It is caused by electron hopping between ferric and ferrous iron. The second mechanism is the ionic conduction (σ_{ionic}), which is derived by migration of vacancies associated with diffusion of structural elements. It is dominated by Mg diffusion because Mg diffuses orders of magnitude faster than Si and O (e.g. Chakraborty et al., 1994; Fei et al., 2012; Fei et al., 2013; Fei et al., 2014; Fei et al., 2018a). The third mechanism is the proton conduction (σ_H), which is driven by the migration of free protons when the crystal contains small amount of water (e.g. Yoshino et al., 2009; Gardés et al., 2014; Zhang and Xia, 2021). The σ_H, σ_{sp}, and σ_{ionic} dominates the electrical conductivity of olivine under relatively low (<1400 K), moderate (1400–1750 K), and high temperature (>1600–1800 K) conditions, respectively (e.g. Schock et al., 1989; Constable et al., 1992; Constable, 2006; Yoshino et al., 2009).

To clarify the contributions of these mechanisms on bulk conductivity of natural olivine under various conditions and thus interpret the electrical conduction profiles in the upper mantle, a number of direct electrical conductivity measurements have been conducted (e.g., Schock et al., 1989; Constable and Duba, 1990; Shankland and Duba, 1990; Constable et al., 1992; Wanamaker and Duba, 1993; Du Frane et al., 2005; Constable, 2006; Wang et al., 2006; Yoshino et al., 2006, 2009; Poe et al., 2010; Yang, 2012; Yoshino et al., 2012; Dai and Karato, 2014a; Dai and Karato, 2014b; Dai and Karato, 2014c; Dai and Karato, 2020; Gardés et al., 2014). Additionally, H and Mg diffusion experiments have been also performed because the proton and ionic conductions can be evaluated using the diffusion coefficients of charge carriers according to the Nernst-Einstein relation (e.g., Hier-Majumder et al., 2005; Du Frane and Tyburczy, 2012; Demouchy et al., 2016; Novella et al., 2017; Fei et al., 2018a; Fei et al., 2018b; Fei et al., 2018c; Sun et al., 2019; Jollands et al., 2020).

Because olivine in the upper mantle contains small amounts of water (e.g. Workman and Hart, 2005; Demouchy and Bolfan-Casanova, 2016), the proton conduction has been previously believed to dominate olivine conductivity under upper mantle conditions for decades. Therefore, it has been extensively investigated as functions of pressure, temperature, oxygen fugacity, iron content, and water content (e.g., Karato, 1990; Wang et al., 2006; Yoshino et al., 2006, 2009; Poe et al., 2010; Yang, 2012; Dai and Karato, 2014a; Dai and Karato, 2014b; Dai and Karato, 2014c; Dai and Karato, 2020; Gardés et al., 2014; Karato, 2019). In contrast, the ionic conduction was overlooked until Fei et al. (2018a), Fei et al. (2020) recently pointed out its significance in the upper mantle. It is therefore necessary to fully understand the ionic conductivity in olivine under various upper-mantle conditions.

* Corresponding author.
E-mail address: hongzhan.fei@uni-bayreuth.de (H. Fei).

https://doi.org/10.1016/j.gsf.2021.101270
1674-9871/

Oxygen fugacity (f_{O_2}), an important parameter in the Earth's mantle, may affect the ionic conductivity (e.g. Wanamaker and Duba, 1993; Du Frane et al., 2005; Constable, 2006), because Mg vacancies can be produced by oxidization of Fe^{2+} to Fe^{3+} in the following reaction (Stock and Smyth, 1978) and enhances Mg diffusion,

$$Mg_{Mg}^{x} + 1/2\ O_2 + 2Fe_{Mg}^{x} = V_{Mg}'' + 2Fe_{Mg}^{\cdot} + MgO \quad (1)$$

Several studies attempted to investigate the f_{O_2} dependence of conductivity in olivine (e.g. Schock et al., 1989; Shankland and Duba, 1990; Wanamaker and Duba, 1993; Du Frane et al., 2005; Constable, 2006) and found f_{O_2} exponents of 1/6 or 2/11. However, those studies were performed at ambient pressure with temperature conditions up to 1870 K. Under such temperature conditions, the electrical conductivity should have been significantly contributed by the small-polaron conduction. Namely, the f_{O_2} dependence of ionic conduction could be affected by the small-polaron conduction. Additionally, the f_{O_2} dependence of conductivity at high pressures could be different from ambient conditions because the ionic and small-polaron conductions have different pressure dependences (Yoshino et al., 2012; Yoshino et al., 2017; Fei et al., 2020). Dai and Karato (2014c), Dai and Karato (2020) reported the f_{O_2} dependence of olivine conductivity at 4 GPa, but only focused on the free-proton conduction regime at relatively low temperatures (870–1270 K).

In this study, we have investigated the f_{O_2} dependence of olivine conductivity at a pressure of 4 GPa and temperatures of 1500–2070 K, which should be in the ionic and small-polaron conduction regimes, with f_{O_2} controlled by the MMO (Mo-MoO_2), RRO (Re-ReO_2), and MH (magnetite-hematite) redox buffers.

2. Experimental procedure

The experimental details are essentially the same as Fei et al. (2020) except for the f_{O_2} buffers. Briefly, handpicked natural olivine single crystals from Pakistan with grain sizes of ~15 mm and Fe/(Mg + Fe) atomic ratio of about 9.0%–9.5% were used as a starting material. They were cut to disks with a 1.0-mm diameter and 0.3-mm thickness in the crystallographic directions of [100], [010], and [001]. Each disk was sandwiched by a pair of Mo, Re, or Pt foils served as electrodes, for MMO, RRO, and MH buffering experiments, respectively, with trace amounts of MoO_2, ReO_2, or Fe_2O_3-Fe_3O_4 near the electrodes in a 18/11 multi-anvil cell assembly. An MgO single crystal in a Mo/Re/Pt shield was used for electrical insulation, namely, the vacancy concentration on Mg sites is minimized. A W75Re25-W97Re3 thermocouple (D-type) was connected to the sample to measure the temperature, and an additional W97Re3 wire was connected to the other side of the sample for conductivity measurements (Fig. 1).

After carefully dried in a vacuum oven at 400 K, each cell assembly was compressed to a pressure of 2 GPa or 4 GPa based on the standard pressure calibration of multi-anvil press at Bayerisches Geoinstitut (Frost et al., 2004; Keppler and Frost, 2005), followed by annealing at 1300 K or 1500 K for a couple of hours until the apparent sample resistance became constant with time. Heating and cooling cycles were sequentially performed at temperatures between 1500 K and 2070 K (Table 1). Higher temperatures were reached in Fei et al. (2020), but at higher pressures). The sample resistance under given temperature conditions was obtained from the complex impedance planes (Fig. 2) collected using a Solartron 1260 Impedance/Gain phase analyzer with the three-wire method. The conductivity (σ) was calculated from the resistance (R), sample diameter (d), and thickness (L), $\sigma = 4L/(\pi d^2 R)$. Only conductivity values repeatable in different heating–cooling cycles were used. The background resistance of the cell assembly was more than one order of magnitude higher than olivine as examined using an Fe-free forsterite sample, whereas the resistance of the thermocouple wire is less than 10 ohm, which is more than two orders of magnitude smaller than olivine. Therefore, the background and resistance of the thermocouple wires have negligible effects on the determination of sample conductivity (Fei et al., 2020).

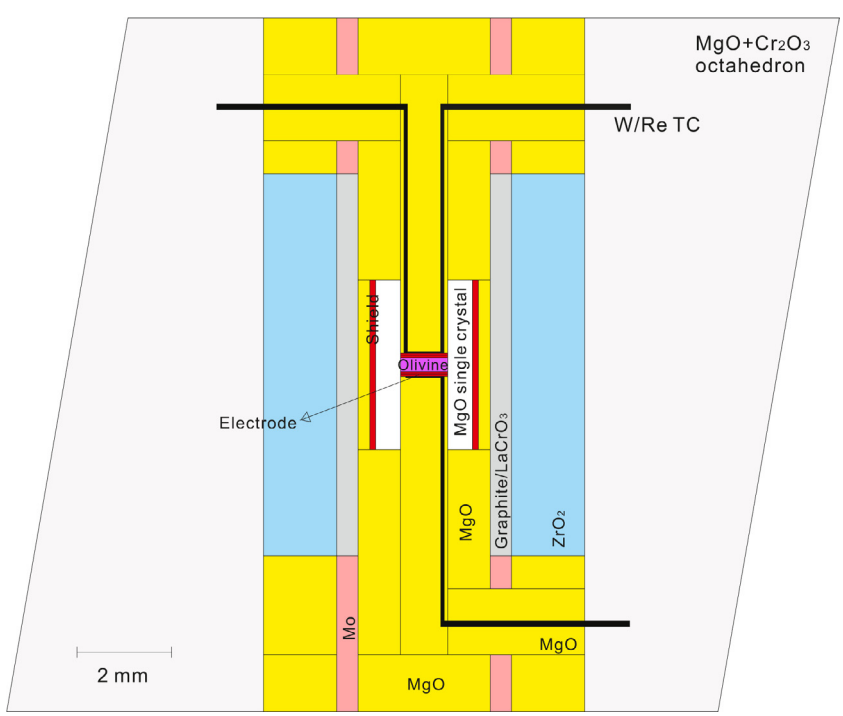

Fig. 1. Cell assembly design used in this study. The Mo, Re, and Pt foils were used as electrodes and shield for the MMO, RRO, and MH buffered experiments, respectively. Graphite furnace was used for MMO and RRO buffered experiments, whereas $LaCrO_3$ was used for MH buffered experiments. Tiny amounts of buffering material power (MoO_2, ReO_2, or Fe_2O_3-Fe_3O_4) was placed near the electrodes. This figure is modified from Fig. 1 of Fei et al. (2020).

Table 1
A list of runs and fitting parameters of $\sigma_{0,ionic}$, $\sigma_{0,sp}$, ΔH_{ionic}, and ΔH_{sp} in Eq. (2). All data are obtained at a pressure of 4 GPa and temperatures of 1500–2070 K. The MMO-buffered runs are already reported in Fei et al. (2020).

Run.No.	axis	f_{O_2} buffer	Fe/(Mg + Fe)	$\log\sigma_{0,ionic}$(K·S/m)	ΔH_{ionic}(kJ/mol)	$\log\sigma_{0,sp}$(S/m)	ΔH_{sp}(kJ/mol)
I471	[100]	MMO	6.6 (4) %	11.6 (1)	353 (6)	1,5 (2)	119 (16)
I477	[100]	RRO	6.1 (6) %	11.9 (13)	367 (4)	2.1 (1)	131 (10)
H4667	[100]	MH	N.D.	12.0 (1)	363 (13)	1.8 (2)	118 (10)
I511	[010]	MMO	N.D.	13.2 (1)	408 (1)	2.7 (2)	162 (26)
H4677	[010]	RRO	7.4 (12) %	13.0 (16)	402 (5)	1.7 (2)	125 (16)
I516	[010]	MH	8.1 (10) %	13.8 (16)	413 (9)	1.7 (1)	122 (6)
H4674	[001]	MMO	8.7 (10) %	13.5 (3)	401 (17)	2.7 (3)	141 (16)
I526	[001]	RRO	10.7 (6) %	13.0 (13)	386 (2)	2.1 (1)	117 (2)
H4663	[001]	MH	8.6 (10) %	12.9 (1)	365 (17)	1.4 (2)	85 (25)

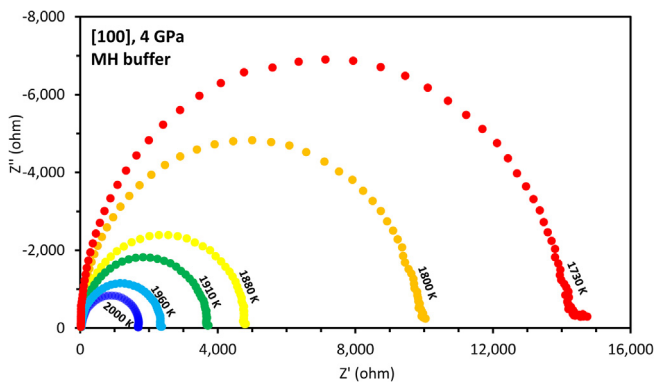

Fig. 2. Examples of complex impedance spectra. The Z' and Z″ are the real and imaginary part of the complex impedance, respectively.

3. Sample characterization

No melt phase was observed in the recovered assemblies by scanning electron microscope analysis (Fig. 3 in this study and Fig. 5 in Fei et al., 2020). It is reasonable because the experimental temperature is lower than the melting point of olivine (~2200 K at 1 atm). Additionally, if melting had occurred, the conductivity-temperature relation should be dramatically curved (Andrault et al., 2018), which was not observed in this study.

The water contents in the recovered samples were about ~20 wt. ppm (Fei et al., 2020). However, it is noted that the uncertainty of the water content estimation could be significant because it is based on unpolarized infrared analysis on the thin section of the recovered assembly with a fixed plane, and the infrared peaks are relatively weak in comparison with the background noisy due to the small water contents (Fei et al., 2020).

The Fe contents in the recovered samples were analyzed using an electron microprobe (Table 2). Because of absorption by electrodes, the Fe contents are different among different samples by a maximum of factor 1.75 (Table 1). However, in the samples with the same crystallographic orientation, the Fe contents are relatively comparable. Therefore, the variation of Fe content in different crystallographic orientations will not significantly affect the f_{O_2} exponent determination in this study.

4. Examination of f_{O_2} in the assembly

Since the solubility of Fe^{3+} in olivine is extremely low, i.e., $Fe^{3+}/\Sigma Fe$ ratio at the level smaller than 10^{-5} (e.g. Canil and O'Neill, 1996; Woodland et al., 2006), it is unable to quantitatively examine the Fe^{3+}/Fe^{2+} ratios in the samples by Mossbauer analysis. Nevertheless, the oxidation of olivine is very fast, which is within

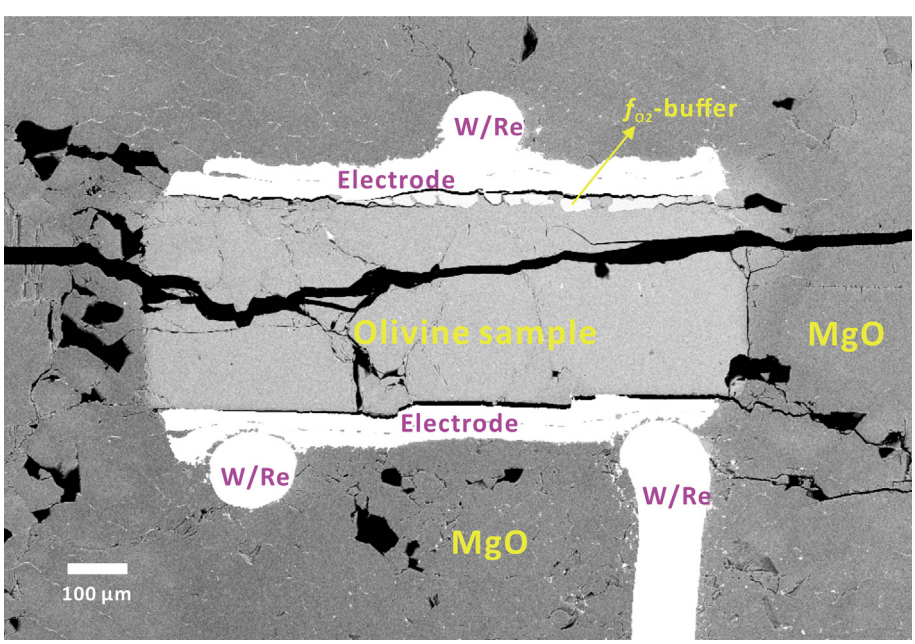

Fig. 3. Example of backscattered scanning electron image of the recovered assembly. No melting of sample or surrounding material was observed in the recovered assembly.

Table 2
Chemical composition of run products. N: number of analyzed grains. The atomic concentration is normalized to O = 24.

Sample	N	MgO (wt.%)	SiO_2 (wt.%)	FeO (wt.%)	Total (wt.%)	Mg (atomic)	Si (atomic)	Fe (atomic)
I526	20	48.57 (43)	40.23 (18)	10.37 (58)	99.16 (35)	10.48 (9)	5.82 (2)	1.25 (7)
H4677	20	50.74 (97)	40.80 (42)	7.23 (119)	98.77 (50)	10.92 (18)	5.89 (3)	0.87 (15)
H4663	21	49.55 (69)	40.34 (23)	8.35 (92)	98.25 (52)	10.74 (14)	5.87 (3)	1.02 (11)
I516	21	50.40 (86)	40.56 (34)	7.88 (99)	98.85 (48)	10.85 (15)	5.86 (3)	0.95 (12)
I477	20	51.46 (46)	41.05 (29)	5.93 (59)	98.44 (42)	11.07 (7)	5.93 (3)	0.72 (7)
H4674	6	50.21 (84)	40.90 (29)	8.51 (100)	99.62 (92)	10.97 (11)	5.99 (4)	1.04 (13)
I471	32	51.65 (34)	41.12 (60)	6.58 (42)	99.36 (88)	11.22 (8)	5.99 (5)	0.80 (5)

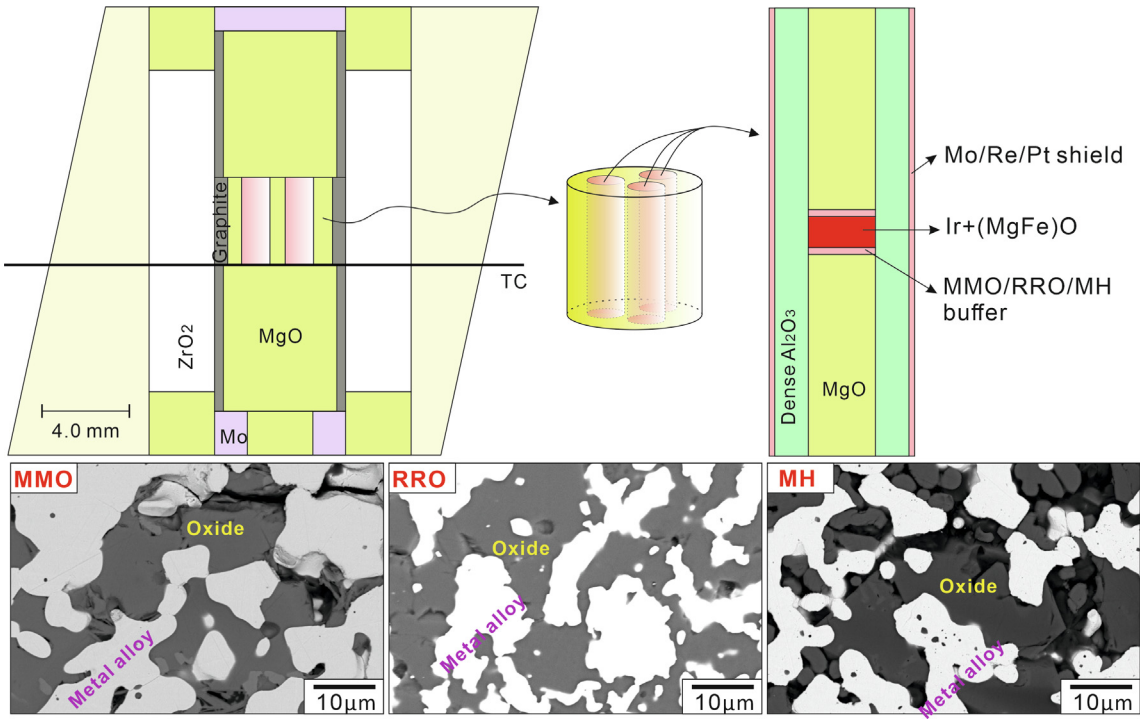

Fig. 4. Examination of f_{O_2} in the assembly. A mixture of Ir and (Mg,Fe)O was sandwiched by the MMO/RRO/MH buffering material in a Mo/Re/Pt shield. The run products appear as coexistences of oxides and metal alloys, with compositions of $Mg_{0.12(1)}Fe_{0.13(1)}Al_{0.04(1)}Mo_{0.21(1)}O_{0.50(1)}$ (oxide) + $Ir_{0.47(1)}Mo_{0.44(2)}Fe_{0.07(1)}O_{0.02(1)}$ (alloy), $Mg_{0.37(1)}Fe_{0.06(1)}Al_{0.03(1)}O_{0.54(1)}$ (oxide) + $Ir_{0.29(6)}Re_{0.70(6)}O_{0.01(1)}$ (alloy), and $Mg_{0.01(1)}Fe_{0.33(2)}Al_{0.10(1)}O_{0.56(1)}$ (oxide) + $Ir_{0.92(1)}Fe_{0.07(1)}O_{0.01(1)}$ (alloy), for the MMO, RRO, and MH buffered conditions, respectively, measured by electron microprobe.

minutes at >1200 K (Knafelc et al., 2019). Namely, the samples should reach the redox state within minutes at high temperatures.

To confirm the f_{O_2}-control in the cell assembly, we performed one additional run using a 25/17 multi-anvil cell assembly, in which a mixture of Ir metal and (Mg,Fe)O (1:1 wt.% ratio) was sandwiched by the MMO, RRO, or MH buffering material, respectively, within a dense Al_2O_3 tube in Mo, Re, or Pt shield in an open system (Fig. 4). This configuration is identical to that for conductivity measurements (Fig. 1). The pressure and temperature conductions of this run is 4 GPa and 1673 K, respectively, with an annealing duration of 5 h, comparable conditions for conductivity measurements. The run products are coexisting oxides and metal alloys. The compositions of oxides are $Mg_{0.12(1)}Fe_{0.13(1)}Al_{0.04(1)}Mo_{0.21(1)}O_{0.50(1)}$, $Mg_{0.37(1)}Fe_{0.06(1)}Al_{0.03(1)}O_{0.54(1)}$, and $Mg_{0.01(1)}Fe_{0.33(2)}Al_{0.10(1)}O_{0.56(1)}$, whereas the metal alloys are $Ir_{0.47(1)}Mo_{0.44(2)}Fe_{0.07(1)}O_{0.02(1)}$, $Ir_{0.29(6)}Re_{0.70(6)}O_{0.01(1)}$, and $Ir_{0.92(1)}Fe_{0.07(1)}O_{0.01(1)}$, for the MMO, RRO, and MH buffered conditions, respectively. The oxides can be assigned as $(Mg,Fe)^{2+}O$ + MoO + Al_2O_3, $(Mg,Fe)^{2+}O$ with some $(Al,Fe)_2^{3+}O_3$ component, and $(Al,Fe)_2^{3+}O_3$ with some $(Mg,Fe)^{2+}O$ component, respectively (Fig. 4). Therefore, the redox state of the samples in the cell assemblies should be buffered under the desired f_{O_2} conditions.

5. Experimental results

As expected, the measured conductivity (σ) systematically increases with increasing temperature (Fig. 5). By plotting the logarithmic σ against the reciprocal temperature (1/*T*), two conduction mechanisms with different temperature dependences were clearly recognized. One mechanism shows a larger temperature dependence appearing at higher temperatures, which was assigned to be the ionic conduction. The second mechanism shows a smaller temperature dependence appearing at lower temperatures, which was assigned to be the small-polaron conduction. The transition from the high-temperature to low-temperature mechanisms occurred at temperatures of approximately 1700–1800 K. The proton conduction was not recognized because the experimental temperatures were relatively high.

In the ionic conduction regime, the conductivity values measured under RRO buffered conditions is comparable as those under MMO buffered conditions, whereas the MH buffered experiments have higher values. In the small-polaron conduction regime, the conductivity gradually increases in the order of MMO-, RRO-, and MH-buffered samples (Fig. 5).

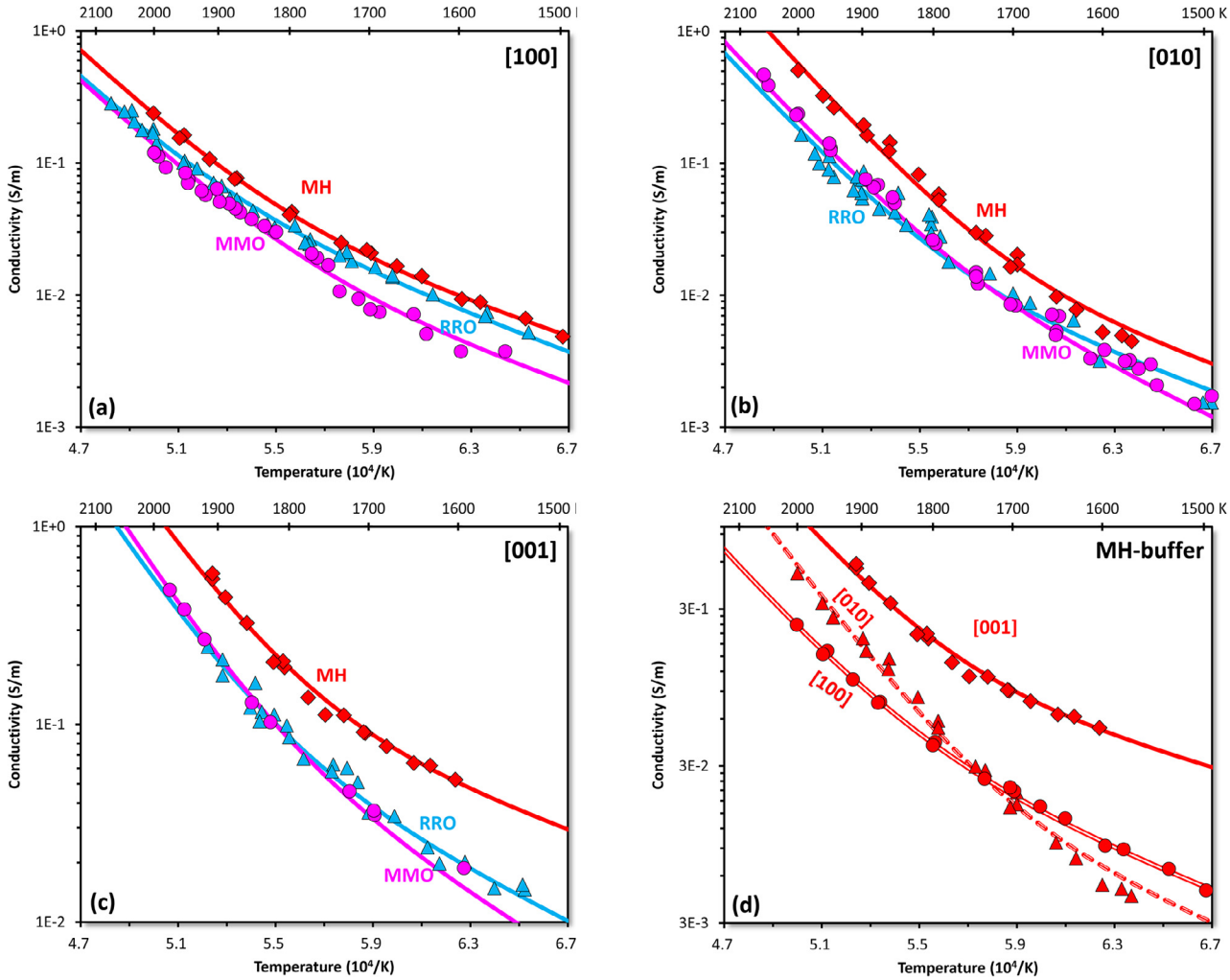

Fig. 5. Experimental results of conductivity in olivine under various f_{O_2} buffer and crystallographic orientation conditions. (a) Along [1 0 0] axis. (b) Along [0 1 0] axis. (c) Along [0 0 1] axis. (d) Comparison along different axis with MH buffer.

The data points from each run are fitted to the Arrhenius equation with ionic (σ_{ionic}) and small-polaron conduction (σ_{sp}) terms,

$$\sigma = \sigma_{ionic} + \sigma_{sp} = \frac{\sigma_{0,ionic}}{T}\exp\left(\frac{\Delta H_{ionic}}{RT}\right) + \sigma_{0,sp}\exp\left(\frac{\Delta H_{sp}}{RT}\right) \quad (2)$$

where σ_0 is the preexponential factor, ΔH is the activation enthalpy, R is the gas constant, T is the absolute temperature, and the subscripted "ionic" and "sp" denote ionic and small-polaron conductions, respectively. The fitting parameters are given in Table 1.

6. Discussion

6.1. Temperature dependences of σ_{ionic} and σ_{sp}

There is no clear f_{O_2}-dependence of both ΔH_{ionic} and ΔH_{sp} (Table 1). The ΔH_{ionic} is 350–410 kJ/mol in all runs, which agrees to the values obtained in previous studies for the ionic conduction (Constable et al., 1992; Constable, 2006; Yoshino et al., 2009; Fei et al., 2020; Table 3). The ΔH_{sp} determined in this study is about 120–160 kJ/mol except run H4663 (Table 1) and agrees to previously obtained enthalpy for the small-polaron conduction (Constable et al., 1992; Xu et al., 1998; Constable, 2006; Yoshino et al., 2009; Yoshino et al., 2012; Table 3). The extremely low ΔH_{sp} in H4663 could be because of the limited data points obtained in the low-temperature regimes. In contrast, the proton conduction usually has an activation energy of less than 100 kJ/mol (e.g. Wang et al., 2006; Yoshino et al., 2006, 2009; Poe et al., 2010; Yang, 2012; Dai and Karato, 2014a; Dai and Karato, 2014b; Dai and Karato, 2014c; Dai and Karato, 2020; Gardés et al., 2014) (Table 3). Therefore, the assignments of high- and low-temperature regimes to ionic and small-polaron conductions, respectively, are robust.

Dai and Karato (2014a) found a regime of conductivity in hydrous olivine with an activation energy of 90–140 kJ/mol at 970–1370 K, higher than that at 570–970 K (71–75 kJ/mol). They attributed their high-temperature regime to the diffusion of $(2H)^{x}_{Mg}$ although the activation energy is comparable with the small-polaron conduction mechanism reported previously (e.g. Constable et al., 1992; Yoshino et al., 2009). Unfortunately, Dai and Karato (2014a) did not reach higher temperatures than 1370 K due to the water loss. The limited experimental temperature range may cause bias of the activation energy in data fitting procedure. Their relatively high activation energy at 970–1370 K could originate from either the small-polaron mechanism, or water-enhanced ionic conduction with much higher activation energy at >1370 K (Fei et al., 2020).

Table 3
Comparison of activation energy, f_{O_2} dependence, and anisotropy of different conduction mechanisms and Mg diffusivity in olivine.

Process	Activation energy (kJ/mol)	f_{O_2} exponent	Anisotropy	References
σ_{ionic}	220–410	0–0.16	[001] > [100] ≈ [010]	This study, Shankland and Duba (1990), Constable et al. (1992), Constable (2006), Yoshino et al. (2009), Yoshino et al. (2017), Fei et al. (2020)
σ_{sp}	120–170	0–0.11	[001] > [100] ≥ [010]	This study, Shankland and Duba (1990), Yoshino et al. (2009), Fei et al. (2020)
$\sigma_{ionic} + \sigma_{sp}^{*a}$	160–170	1/6 to 2/11	[001] > [100] ≥ [010]	Schock et al. (1989), Xu et al. (1998), Du Frane et al. (2005)
σ_H	<100	−0.1 to 0.1	Inconsistent with each other	Wang et al. (2006), Yoshino et al. (2006), Yoshino et al. (2009), Poe et al. (2010), Yang (2012), Dai and Karato (2014a), Dai and Karato (2014b), Dai and Karato (2014c), Dai and Karato (2020)
Mg diffusion	220–400	0 to 1/6	[001] > [100] ≈ [010]	Chakraborty et al. (1994), Hier-Majumder et al. (2005), Fei et al. (2018a), Jollands et al. (2020)

*a: Only the bulk conductivity is reported in some studies without separation of different mechanisms (Schock et al., 1989; Xu et al., 1998; Du Frane et al., 2005).

6.2. Anisotropy of σ_{ionic} and σ_{sp}

As already discussed in previous studies (e.g., Schock et al., 1989; Constable et al., 1992; Du Frane et al., 2005; Fei et al., 2020), both the ionic and small-polaron conductions in olivine have strong anisotropy. The conductivity anisotropy is also observed in this study: the σ_{ionic} along [001] axis ($\sigma_{ionic[001]}$) is higher than $\sigma_{ionic[100]}$ and $\sigma_{ionic[010]}$ by ~0.5 orders of magnitude under any buffer conditions, whereas $\sigma_{ionic[010]}$ is slightly higher than $\sigma_{ionic[100]}$ under MH buffered condition (Figs. 5d and 6a), and comparable under MMO-buffered condition (Fei et al., 2020). Therefore, we have $\sigma_{ionic[001]} > \sigma_{ionic[010]} \approx \sigma_{ionic[100]}$. It can be explained by the distance of Mg sites along different crystallographic directions in the crystal structure of olivine. The M1 site, which is the dominant site for Mg vacancies and therefore dominates Mg diffusion in olivine (Ottonello et al., 1990; Brodholt, 1997), has the distance in the order of [010] >≈ [100] ≫ [001] (Fig. 7). This order is opposite of conductivity and Mg diffusivity (both are [001] ≫ [100] >≈ [010] (Constable et al., 1992; Chakraborty et al., 1994; Du Frane et al., 2005; Jollands et al., 2020 as shown in Table 3), which is reasonable because longer distance between M1 sites will cause more difficulty for migration of Mg ions/vacancies.

The anisotropy is also observed in the small-polaron conduction regime with an order of $\sigma_{sp[001]} > \sigma_{sp[100]} >\approx \sigma_{sp[010]}$ (Fig. 6b; Table 3), which agrees with the ambient pressure data (Shankland and Duba, 1990; Constable et al., 1992; Du Frane et al., 2005). Since σ_{sp} is driven by the hopping of electrons between Fe^{2+} and Fe^{3+}, it should be inversely proportional to the distances between Fe ions, thus also correlated to distance of Mg site along the crystallographic axes by assuming homogeneous distribution of Fe^{x}_{Mg} and $Fe^{\bullet}_{Mg}$ in Mg sites. Therefore, the order of $_{sp[001]} > \sigma_{sp[100]} >\approx \sigma_{sp[010]}$ should be the same as those for σ_{ionic} as experimentally observed in this and previous studies (e.g. Constable et al., 1992; Du Frane et al., 2005; Table 3).

6.3. f_{O_2} dependences of σ_{ionic} and σ_{sp}

By applying the fitting parameters listed in Table 1 to Eq. (1), the simulated values of σ_{ionic}, σ_{sp}, and bulk conductivity ($\sigma_{ionic} + \sigma_{sp}$) at 1700 K are plotted against f_{O_2} in Fig. 6, where the f_{O_2} values for MMO, RRO, FMQ, and MH buffers are calculated according to the reported thermodynamic data (Chou, 1978; O'Neill, 1986; O'Neill, 1987; Pownceby and O'Neill, 1994). As shown in Fig. 6, both σ_{ionic} and σ_{sp} are f_{O_2}-independent under low f_{O_2} conditions, but f_{O_2}-dependent at higher f_{O_2}, with the f_{O_2} exponent of r = −0.02 to 0.06 and 0.03–0.16, respectively, in the relation of $\sigma \propto {f_{O_2}}^{r}$ (Fig. 6a, b). As a result, the bulk conductivity ($\sigma_{ionic} + \sigma_{sp}$) follows similar f_{O_2} dependences as σ_{ionic} and σ_{sp} (Fig. 6c). Note that the slightly negative r (−0.01 to −0.02) for $\sigma_{ionic[100]}$ and $\sigma_{ionic[[010]}$ in Fig. 6a is probably caused by experimental uncertainty.

Constable (2006) proposed the f_{O_2} effect of standard olivine conductivity model with two terms, $\sigma = \sigma_{Fe^{\bullet}_{Mg}} + \sigma_{V''_{Mg}}$, corresponding to the $Fe^{\bullet}_{Mg}$ controlled small-polaron conduction and V''_{Mg} controlled ionic conduction, respectively, in the f_{O_2} range from IW (iron-wüstite, which is close to MMO buffer) to FMQ (fayalite-magnetite-quartz). Because $[Fe^{\bullet}_{Mg}] \propto {f_{O_2}}^{1/6}$ and $[V''_{Mg}] \propto {f_{O_2}}^{1/6}$ in olivine (Stocker and Smyth, 1978), both σ_{ionic} and σ_{sp} are assumed to have an f_{O_2} exponent of 1/6 in Constable (2006)'s model. As shown in Fig. 6, the ionic conductivity at 1700 K given by Constable (2006) is higher than that of isotropic model determined in this study (Fig. 6a), whereas the small polaron conductivity is lower (Fig. 6b). In contrast, the bulk conductivity of Constable (2006) and this study are comparable (Fig. 6c). This is probably because Constable (2006)'s model is based on experimental data points obtained at a limited temperature range (1370–1570 K), under the temperature conditions that both small polaron and ionic mechanisms contribute significantly to the bulk conductivity. As a result, the two mechanisms and their f_{O_2}-dependences cannot be precisely extracted from the bulk conductivity.

Du Frane et al. (2005) experimentally investigated the effect of f_{O_2} on olivine conductivity at ambient pressure with f_{O_2} in the range from FMQ − 2 to FMQ + 3, and found the f_{O_2}-indepdnent regime under relatively reducing conditions and $\sigma \propto {f_{O_2}}^{\frac{2}{11}\sim\frac{1}{6}}$ at f_{O_2} close to or higher than FMQ buffer. Du Frane et al. (2005) attributed this f_{O_2}-indepdnent regime to impurity, the concentration of which is insensitive to f_{O_2}. This could also be the case of our high-pressure experiments. One reason is that natural olivine always contains small amount of trace elements, e.g., H, Cr, Ti (Gose et al. 2010). Such trace elements will produce V''_{Mg} and $Fe^{\bullet}_{Mg}$ independently from f_{O_2} conditions. We expect that when f_{O_2} is low, V''_{Mg} and $Fe^{\bullet}_{Mg}$ are dominantly produced by impurities. Therefore, small-polaron and ionic conductions will consequentially have no f_{O_2} dependence. In contrast, with high f_{O_2}, the majority of V''_{Mg} and $Fe^{\bullet}_{Mg}$ are produced by oxidization of ferrous iron as described in Eq. (1). As a result, both σ_{ionic} and σ_{sp} follow similar f_{O_2} dependence. The f_{O_2}-dependent regime in this study occurred at higher f_{O_2} condition than Constable (2006) and Du Frane et al. (2005) (Fig. 6). This is reasonable because the samples may absorb

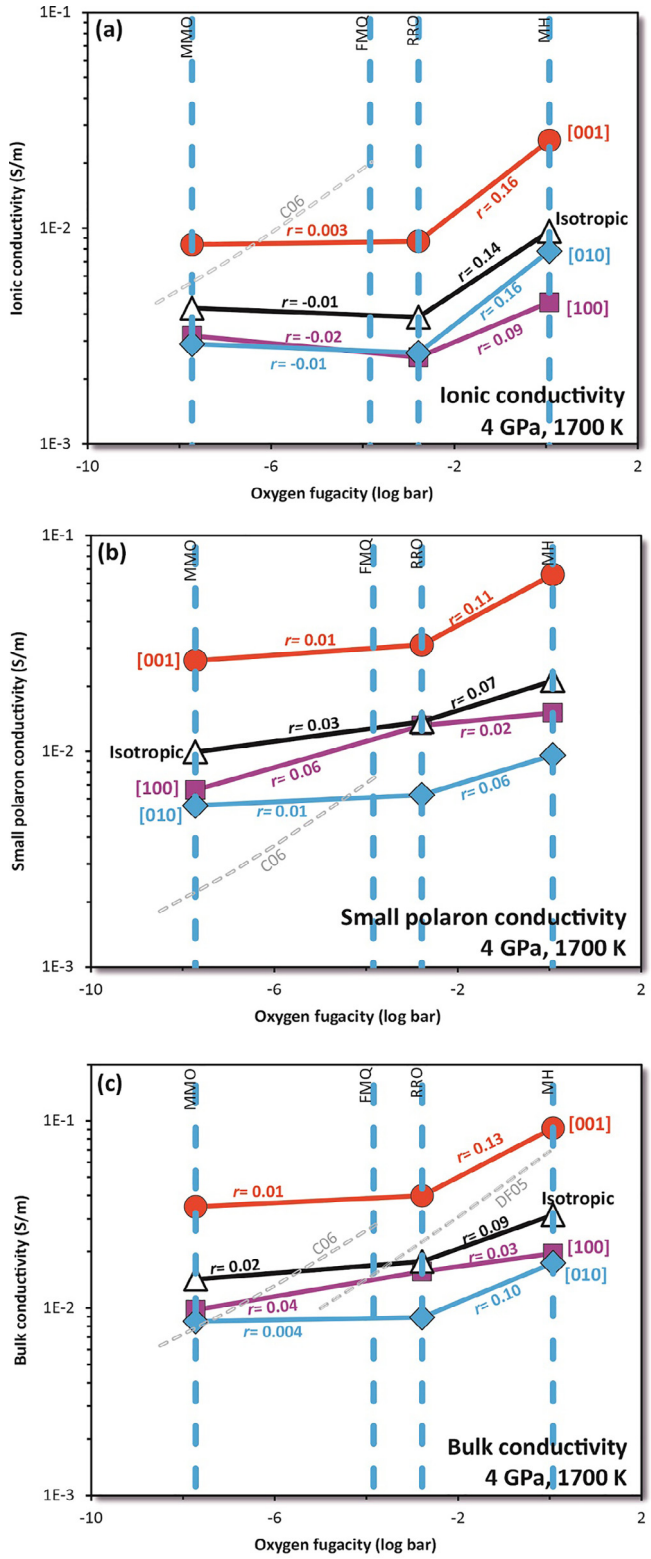

Fig. 6. Simulated conductivity at various f_{O_2} conditions from Eq. (1) using the parameters given in Table 1. (a) Pure ionic conduction. (b) Pure small-polaron conduction. (c) Bulk conductivity by the summation of $\sigma_{ionic} + \sigma_{sp}$. The isotropic model is obtained from the geometric mean of [100], [010], and [001] axes, i.e., $\sigma_{isotropic} = (\sigma_{[100]} \times \sigma_{[010]} \times \sigma_{[001]})^{1/3}$. All data are corrected to a temperature of 1700 K. The r is the f_{O_2} exponent in the relation $\sigma \propto f_{O_2}^{r}$ obtained by linear functions of the data points. C06: Constable (2006) with f_{O_2} in the range from IW to FMQ. DF05: Du Frane et al. (2005) with f_{O_2} in the range from FMQ-2 to FMQ + 3.

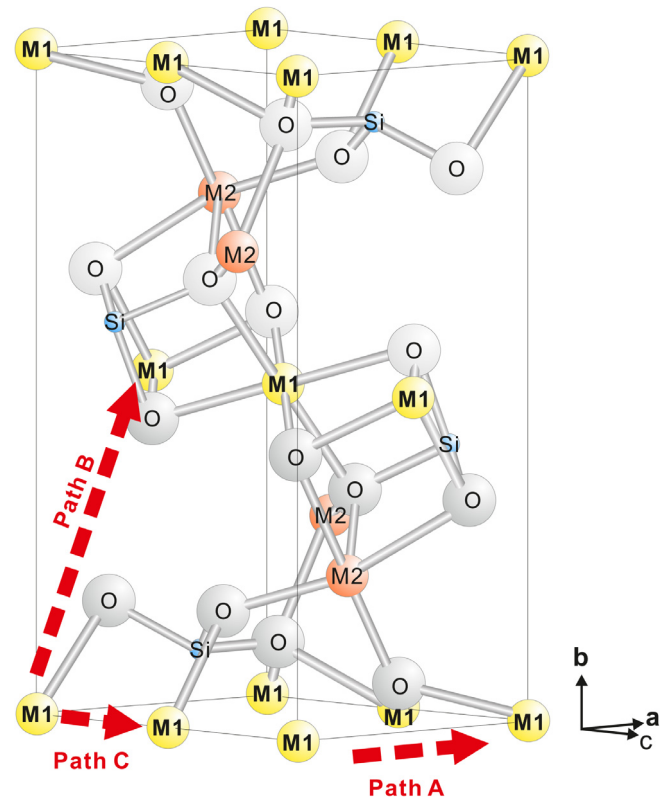

Fig. 7. Hopping distance of M1 site in a unit cell of olivine. The Path A, B, and C indicate the shortest hopping distances for M1 site in [100], [010], and [001] directions, which are a, $\frac{1}{2}\sqrt{a^2+b^2}$, and $\frac{1}{2}c$, respectively. Fe-bearing olivine has a = 4.75 Å, b = 10.19 Å, c = 5.98 Å under ambient pressure conditions (Hazen, 1976).

additional trace elements from the surrounding materials in high pressure experiments.

6.4. Geophysical implications

Magnetotellurical observations (Evans et al., 2005; Baba et al., 2006) reported a high electrical conductivity layer at the topmost asthenosphere about ~70–120 km depth (2–4 GPa) near the East Pacific Rise (Fig. 8). The origin of this high conductivity anomaly has been debated for decades and different models have been suggested (e.g. Karato, 1990; Karato, 2019; Wang et al., 2006; Yoshino et al., 2006, 2009; Poe et al., 2010; Dai and Karato, 2014a; Gardés et al., 2014; Katsura and Fei, 2021). However, no definite conclusion has been obtained. That is because, despite the high temperature conditions in the asthenosphere, most previous studies focused on the proton conduction at relatively low temperature conditions. As proved experimentally (e.g. Yoshino et al., 2009), the proton conduction may dominate olivine conductivity only at relatively low temperature conditions, i.e., <1400 K, distinctively lower than the geotherm in the asthenosphere at 70–120 km depth beneath young plates, i.e. 1600–1700 K (Katsura et al., 2017).

In contrast to those studies, we have paid attention to the ionic conductivity (Fei et al., 2018a; Fei et al., 2020). According to temperature and crystallographic orientation dependences of σ_{ionic} determined in this study, we can draw a bulk conductivity profile of olivine ($\sigma_i + \sigma_{sp}$) at 4 GPa under each buffer conditions (MMO, RRO, and MH) at asthenospheric temperatures. As shown in Fig. 8, when f_{O_2} is close to MMO or RRO buffered conditions, the bulk

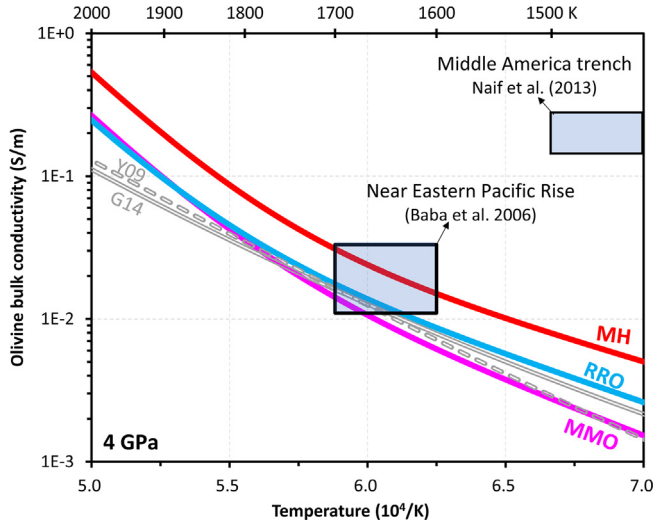

Fig. 8. Electrical conductivity of olivine with MMO, RRO, and MH buffer at 4 GPa corresponding to the topmost asthenosphere conditions. The models given by Y09 (Yoshino et al., 2009) and G14 (Gardés et al., 2014) are also shown for comparison after water contents adjusted to 20 wt. ppm for the free proton conduction and no adjustment for the ionic conduction.

conductivity is identical to those reported by Yoshino et al. (2009) and Gardés et al. (2014) under comparable conditions with ~20 wt ppm water since our samples may contain ~20 wt. ppm water as well (Fei et al., 2020). At 1600–1700 K, corresponding to the temperatures in the asthenosphere beneath 5 Ma age plates (Katsura et al., 2017)], the bulk conductivity under MMO or RRO buffered conditions is slightly smaller than that observed near East Pacific Rise (Baba et al., 2006; Evans et al., 2005). However, when f_{O_2} is close to the MH buffer, the bulk conductivity is comparable with the observed values (Fig. 8). Additionally, the incorporation of ~60 wt. ppm water of in olivine in the asthenosphere (Demouchy and Bolfan-Casanova, 2016) and enlargement of Mg diffusivity by pyroxene buffer (Jollands et al., 2020) will further enhance the contribution of ionic conduction mechanism to the bulk conductivity in olivine. The high conductivity layer in the asthenosphere near East Pacific Rise therefore can be interpreted by the bulk conductivity of olivine that significantly contributed by ionic mechanism under relatively oxidized conditions and/or enhanced by water and pyroxene-buffer.

Thus, the bulk conductivity of olivine under relatively oxidized conditions fits well with the conductivity profile in the topmost asthenosphere. Presence of carbonatite melts or peridotitic melts under shear deformation may further raise the conductivity in the asthenosphere (e.g. Gaillard et al., 2008; Caricchi et al. 2011; Zhang et al., 2014; Zhang et al., 2021; Pommier et al., 2015; Naif, 2018; Zhang and Yoshino, 2020), however, they are only required in the regions with extremely high conductivity values, i.e., >0.1 S/m at 45–70 km depth beneath Middle America trench (Naif et al., 2013) (Fig. 8).

Declaration of Competing Interest

The authors declare that they have no known competing financial interests or personal relationships that could have appeared to influence the work reported in this paper.

Acknowledgments

We thank S. Linhardt for technical assistance of in-situ impedance analysis, R. Njul for sample preparation, H. Fisher for machining high-pressure cell assemblies, D. Krauße for assistance in EPMA analysis, and two anonymous reviewers for helpful comments. This work is financially supported by the annual budget of Bayerisches Geoinstitut to H. Fei and the German Research Foundation (DFG) to T. Katsura (KA3434/3-1, KA3434/3-2, KA3434/7-1, KA3434/8-1, and KA3434/9-1).

References

Andrault, D., Pesce, G., Manthilake, G., Monteux, J., Bolfan-Casanova, N., Chantel, J., Novella, D., Guignot, N., King, A., Itié, J.-P., Hennet, L., 2018. Deep and persistent melt layer in the Archaean mantle. Nat. Geosci. 11 (2), 139–143.
Baba, K., Chave, A.D., Evans, R.L., Hirth, G., Mackie, R.L., 2006. Mantle dynamics beneath the East Pacific Rise at 17oS: insights from the mantle electromagnetic and tomography (MELT) experiment. J. Geophys. Res. 111, B02101.
Brodholt, J., 1997. Ab initio calculations on point defects in forsterite (Mg_2SiO_4) and implications for diffusion and creep. Am. Min. 82, 1049–1053.
Canil, D., O'Neill, H.S.C., 1996. Distribution of ferric iron in some upper-mantle assemblages. J. Petrol. 37, 609–635.
Caricchi, L., Gaillard, F., Mecklenburgh, J., Le Trong, E., 2011. Experimental determination of electrical conductivity during deformation of melt-bearing olivine aggregates: implications for electrical anisotropy in the oceanic low velocity zone. Earth Planet. Sci. Lett. 302, 81–94.
Chakraborty, S., Farver, J.R., Yund, R.A., Rubie, D.C., 1994. Mg tracer diffusion in synthetic forsterite and San Carlos olivine as a function of P, T, and fO_2. Phys. Chem. Miner. 21, 489–500.
Chou, I.M., 1978. Calibration of oxygen buffers at elevated P and T using the hydrogen fugacity sensor. Am. Min. 63, 690–703.
Constable, S., Duba, A., 1990. Electrical conductivity of olivine, a dunite, and the mantle. J. Geophys. Res. 95, 6967–6978.
Constable, S., Shankland, T.J., Duba, A., 1992. The electrical conductivity of an isotropic olivine mantle. J. Geophys. Res. 97, 3397–3404.
Constable, S., 2006. SEO3: A new model of olivine electrical conductivity. Geophys. J. Int. 166, 435-437.
Dai, L., Karato, S.I., 2014a. High and highly anisotropic electrical conductivity of the asthenosphere due to hydrogen diffusion in olivine. Earth Planet. Sci. Lett. 408, 79–86.
Dai, L., Karato, S.-I., 2014b. The effect of pressure on the electrical conductivity of olivine under the hydrogen-rich conditions. Phys. Earth Planet. Int. 232, 51–56.
Dai, L., Karato, S.-I., 2014c. Influence of oxygen fugacity on the electrical conductivity of hydrous olivine: Implications for the mechanism of conduction. Phys. Earth Planet. Int. 232, 57–60.
Dai, L., Karato, S.I., 2020. Electrical conductivity of Ti-bearing hydrous olivine aggregates at high temperature and high pressure. J. Geophys. Res. 125, e2020JB020309.
Demouchy, S., Bolfan-Casanova, N., 2016. Distribution and transport of hydrogen in the lithospheric mantle: A review. Lithos 240, 402–425.
Demouchy, S., Thoraval, C., Bolfan-Casanova, N., Manthilake, G., 2016. Diffusion of hydrogen in iron-bearing olivine at 3 GPa. Phys. Earth Planet. Int. 260, 1–13.
Du Frane, W.L., Roberts, J.J., Toffelmier, D.A., Tyburczy, J.A., 2005. Anisotropy of electrical conductivity in dry olivine. Geophys. Res. Lett. 32, L24315.
Du Frane, W.L., Tyburczy, J.A., 2012. Deuterium-hydrogen exchange in olivine: implications for point defects and electrical conductivity. Geochem. Geophys. Geosyst. 13, Q03004.
Evans, R.L., Hirth, G., Baba, K., Forsyth, D., Chave, A., Mackie, R., 2005. Geophysical evidence from the MELT area for compositional controls on oceanic plates. Nature 437, 249–252.
Fei, H., Hegoda, C., Yamazaki, D., Wiedenbeck, M., Yurimoto, H., Shcheka, S., Katsura, T., 2012. High silicon self-diffusion coefficient in dry forsterite. Earth Planet. Sci. Lett. 345, 95–103.
Fei, H., Wiedenbeck, M., Yamazaki, D., Katsura, T., 2013. Small effect of water on upper mantle rheology based on Si self-diffusion coefficients. Nature 498, 213–215.
Fei, H., Wiedenbeck, M., Yamazaki, D., Katsura, T., 2014. No effect of water on oxygen self-diffusion rate in forsterite. J. Geophys. Res. 119, 7598–7606.
Fei, H., Koizumi, S., Sakamoto, N., Hashiguchi, M., Yurimoto, H., Marquardt, K., Miyajima, N., Katsura, T., 2018a. Mg lattice diffusion in iron-free olivine and implications to conductivity anomaly in the oceanic asthenosphere. Earth Planet. Sci. Lett. 484, 204–212.
Fei, H., Koizumi, S., Sakamoto, N., Hashiguchi, M., Yurimoto, H., Marquardt, K., Miyajima, N., Katsura, T., 2018b. Pressure, temperature, water content, and oxygen fugacity dependence of the Mg grain-boundary diffusion coefficient in forsterite. Am. Min. 103, 1354–1361.
Fei, H., Wiedenbeck, M., Sakamoto, N., Yurimoto, H., Yoshino, T., Yamazaki, D., Katsura, T., 2018c. Negative activation volume of oxygen self-diffusion in forsterite. Phys. Earth Planet. Int. 275, 1–8.
Fei, H., Druzhbin, D., Katsura, T., 2020. The effect of water on ionic conductivity in olivine. J. Geophys. Res. 125, e2019JB019313.
Frost, D.J., Poe, B.T., Trønnes, R.G., Liebske, C., Duba, A., Rubie, D.C., 2004. A new large-volume multianvil system. Phys. Earth Planet. Int. 143, 507–514.
Gaillard, F., Malki, M., Iacono-Marziano, G., Pichavant, M., Scaillet, B., 2008. Carbonatite melts and electrical conductivity in the asthenosphere. Science 322, 1363–1365.

Gardés, E., Gaillard, F., Tarits, P., 2014. Toward a unified hydrous olivine electrical conductivity law. Geochem. Geophys. Geosys. 15, 4984–5000.
Gose, J., Schmädicke, E., Markowitz, M., Beran, A., 2010. OH point defects in olivine from Pakistan. Miner Petrol. 99, 105–111.
Hazen, R.M., 1976. Effects of temperature and pressure on the crystal structure of forsterite. Am. Min. 61, 1280–1293.
Hier-Majumder, S., Anderson, I.M., Kohlstedt, D.L., 2005. Influence of protons on Fe-Mg interdiffusion in olivine. J. Geophys. Res. 110, B02202.
Jollands, M.C., Zhukova, I., O'Neill, H.S.C., Hermann, J., 2020. Mg diffusion in forsterite from 1250–1600° C. Am. Min. 105, 525–537.
Karato, S., 1990. The role of hydrogen in the electrical conductivity of the upper mantle. Nature 347, 272–273.
Karato, S., 2019. Some remarks on hydrogen-assisted electrical conductivity in olivine and other minerals. Progress Earth Planet. Sci. 6, 55. https://doi.org/10.1186/s40645-019-0301-2.
Katsura, T., Baba, K., Yoshino, T., Kogiso, T., 2017. Electrical conductivity of the oceanic asthenosphere and its interpretation based on laboratory measurements. Tectonphys. 717, 162–181.
Katsura, T., Fei, H., 2021. Asthenosphere dynamics based on the H_2O dependence of element diffusivity in olivine. Natl. Sci. Rev. 8, nwaa278.
Keppler, H., Frost, D.J., 2005. Introduction to minerals under extreme conditions. EMU Notes in Mineralogy, vol. 7, Chapter 1, pp. 1–30.
Knafelc, J., Filiberto, J., Ferré, E.C., Conder, J.A., Costello, L., Crandall, J.R., Dyar, M.D., Friedman, S.A., Hummer, D.R., Schwenzer, S.P., 2019. The effect of oxidation on the mineralogy and magnetic properties of olivine. Am. Min. 104, 694–702.
Naif, S., Key, K., Constable, S., Evans, R.L., 2013. Melt-rich channel observed at the lithosphere-asthenosphere boundary. Nature 495, 356–359.
Naif, S., 2018. An upper bound on the electrical conductivity of hydrated oceanic mantle at the onset of dehydration melting. Earth Planet. Sci. Lett. 482, 357–366.
Novella, D., Jacobsen, B., Weber, P.K., Tyburczy, J.A., Ryerson, F.J., Du Frane, W.L., 2017. Hydrogen self-diffusion in single crystal olivine and electrical conductivity of the Earth's mantle. Sci. Rep. 7, 5344.
O'Neill, H.S.C., 1986. Mo-MoO_2 (MOM) oxygen buffer and the free energy of formation of MoO_2. Am. Min. 71, 1007–1010.
O'Neill, H.S.C., 1987. Quartz-fayalite-iron and quartz-fayalite-magnetite equilibria and the free energy of formation of fayalite (Fe_2SiO_4) and magnetite (Fe_3O_4). Am. Min. 72, 67–75.
Ottonello, G., Princivalle, F., Della Giusta, A., 1990. Temperature, composition, and f_{O2} effects on intersite distribution of Mg and Fe^{2+} in olivines. Phys. Chem. Min. 17, 301–312.
Poe, B.T., Romano, C., Nestola, F., Smyth, J.R., 2010. Electrical conductivity anisotropy of dry and hydrous olivine at 8 GPa. Phys. Earth Planet. Int. 181, 103–111.
Pommier, A., Leinenweber, K., Kohlstedt, D.L., Qi, C., Garnero, E.J., Mackwell, S.J., Tyburczy, J.A., 2015. Experimental constraints on the electrical anisotropy of the lithosphere-asthenosphere system. Nature 522, 202–206.
Pownceby, M.I., O'Neill, H.S.C., 1994. Thermodynamic data from redox reactions at high temperatures. IV. Calibration of the Re-ReO_2 oxygen buffer from EMF and NiO + Ni-Pd redox sensor measurements. Contrib. Miner. Petrol. 118, 130–137.
Schock, R.N., Duba, A.G., Shankland, T.J., 1989. Electrical conduction in olivine. J. Geophys. Res. 94, 5829–5839.
Shankland, T.J., Duba, A.G., 1990. Standard electrical conductivity of isotropic, homogeneous olivine in the temperature range 1200°–1500 °C. Geophys. J. Int. 103, 25–31.
Stocker, R.L., Smyth, D.M., 1978. Effect of enstatite activity and oxygen partial pressure on the point-defect chemistry of olivine. Phys. Earth Planet. Int. 16, 145–156.
Sun, W., Yoshino, T., Kuroda, M., Sakamoto, N., Yurimoto, H., 2019. H-D interdiffusion in single-crystal olivine: implications for electrical conductivity in the upper mantle. J. Geophys. Res. 124, 5696–5707.
Wanamaker, B.J., Duba, A.G., 1993. Electrical conductivity of San Carlos olivine along [100] under oxygen- and pyroxene-buffered conditions and implications for defect equilibria. J. Geophys. Res. 98, 489–500.
Wang, D., Mookherjee, M., Xu, Y., Karato, S.-I., 2006. The effect of water on the electrical conductivity of olivine. Nature 443, 977–980.
Woodland, A.B., Kornprobst, J., Tabit, A., 2006. Ferric iron in orogenic lherzolite massifs and controls of oxygen fugacity in the upper mantle. Lithos 89, 222–241.
Workman, R.K., Hart, S.R., 2005. Major and trace element composition of the depleted MORB mantle (DMM). Earth Planet Sci. Lett. 231, 53–72.
Xu, Y., Poe, B.T., Shankland, T.J., Rubie, D.C., 1998. Electrical conductivity of olivine, wadsleyite, and ringwoodite under upper-mantle conditions. Science 280, 1415–1418.
Yang, X., 2012. Orientation-related electrical conductivity of hydrous olivine, clinopyroxene and plagioclase and implications for the structure of the lower continental crust and uppermost mantle. Earth Planet. Sci. Lett. 317, 241–250.
Yoshino, T., Matsuzaki, T., Yamashita, S., Katsura, T., 2006. Hydrous olivine unable to account for conductivity anomaly at the top of the asthenosphere. Nature 443, 973–976.
Yoshino, T., Matsuzaki, T., Shatskiy, A., Katsura, T., 2009. The effect of water on the electrical conductivity of olivine aggregates and its implications for the electrical structure of the upper mantle. Earth Planet. Sci. Lett. 288, 291–300.
Yoshino, T., Shimojuku, A., Shan, S., Guo, X., Yamazaki, D., Ito, E., Higo, Y., Funakoshi, K.-I., 2012. Effect of temperature, pressure and iron content on the electrical conductivity of olivine and its high-pressure polymorphs. J. Geophys. Res. 117, B08205.
Yoshino, T., Zhang, B., Rhymer, B., Zhao, C., Fei, H., 2017. Pressure dependence of electrical conductivity in forsterite. J. Geophys. Res. 122, 158–171.
Zhang, B., Yoshino, T., Yamazaki, D., Manthilake, G., Katsura, T., 2014. Electrical conductivity anisotropy in partially molten peridotite under shear deformation. Earth Planet. Sci. Lett. 405, 98–109.
Zhang, B., Yoshino, T., 2020. Temperature-enhanced electrical conductivity anisotropy in partially molten peridotite under shear deformation. Earth Planet. Sci. Lett. 530, 115922.
Zhang, B., Guo, X., Yoshino, T., Xia, Q., 2021. Electrical conductivity of melts: implications for conductivity anomalies in the Earth's mantle. National Sci. Rev., nwab064 https://doi.org/10.1093/nsr/nwab064.
Zhang, B.-H., Xia, Q.-K., 2021. Influence of water on the physical properties of olivine, wadsleyite, and ringwoodite. Eur. J. Miner. 33, 39–75.